ELSEVIER

Chemical Engineering Journal 140 (2008) 398–413

Chemical Engineering Journal

www.elsevier.com/locate/cej

Analysis of the bubbling behaviour of 2D gas solid fluidized beds Part I. Digital image analysis technique

Antonio Busciglio, Giuseppa Vella, Giorgio Micale *, Lucio Rizzuti

Dipartimento di Ingegneria Chimica dei Processi e dei Materiali, Facoltà di Ingegneria, Università degli Studi di Palermo, Viale delle Scienze Ed. 6, Palermo 90128, Italy

Received 28 May 2007; received in revised form 7 November 2007; accepted 9 November 2007

Abstract

Bubble characteristics are very important in the design of fluidized beds because they govern hydrodynamics and efficiency of the operation for which the bed is used. In this work, a digital image analysis technique has been developed to study the fluidization dynamics of a lab-scale two-dimensional bubbling bed. Digital image analysis may supply a great quantity of information; it is non-intrusive, capable of securing several properties simultaneously and cost effective. The image analysis method here developed allows for the simultaneous measurements of various significant bubble properties, i.e. bubble size and bubble velocity distributions, bed height and bubble-phase hold-up, by means of a purposely in-house developed software. Present results were compared with relevant literature correlations and resulted in sound agreement, thus confirming the large potential of the technique here developed.

Keywords: Image analysis; Bubbles; Fluidization

1. Introduction and literature review

In recent years, scientific research focused on industrial engineering issues has been largely benefiting from the huge increase of computing power made available by state of the art computers. Computational procedures which were considered, until a few years ago, not viable even on large mainframes, are now effortlessly run on commercial desktop computers.

Therefore, numerical simulations of more and more complex systems may today be successfully tackled. In particular, it is possible to run and validate complex models for the description of physico-chemical phenomena occurring into equipments operating under virtually any regime, for the case of single-phase or even multi-phase systems. Moreover, the possibility of devising more and more sophisticated mathematical models allows to analyze industrial equipments with higher modelling and computational requirements.

The above considerations allow to state the large potential to investigate complex fluidization dynamics, such as that of bubbling regimes, by means of mathematical modelling and numerical simulation.

However, in order to fully validate relevant models and methods it is necessary to get accurate and detailed quantitative experimental information, purposely collected for the task.

It is the aim of the present work to specifically develop a technique useful for the analysis of bubbling fluidization on the basis of digital image processing, which in fact may well perform a rigorous and highly detailed assessment of experimental data and may even be adopted for the analysis of computational results conveniently expressed into image graphics. Of course from stringent comparison between model and experimental results, it will then be possible to further develop and strengthen the modelling work.

The principal difficulty in analyzing fluidization quality and bubble dynamic is concerned with the possibility of measuring the physical and geometrical properties of the gas bubbles rising in a solid granular medium.

As a matter of fact, the gas flow in excess of that required to maintain the dense phase at minimum fluidization conditions flows through the bed in the form of bubbles and through flow [1]. Increasing the flow above the minimum bubbling velocity encourages more bubbles of larger size to nucleate in the bed,

* Corresponding author. Tel.: +39 0916567310; fax: +39 0916567280.
E-mail address: micale@dicpm.unipa.it (G. Micale).

1385-8947/$ – see front matter © 2007 Elsevier B.V. All rights reserved.
doi:10.1016/j.cej.2007.11.015

Nomenclature

A_0	catchment area of distributor (cm^2)
A_b	bubble area (cm^2)
$b(x,y)$	pixel luminance of a single object
d_b	bubble equivalent diameter (cm)
$f_n(x,y)$	matrix representation of frame nth
F	frame number
g	acceleration due to gravity (cm/s^2)
$g(x,y)$	pixel luminance in binary image
$G(x,y)$	bubble phase indicator
h	bubble height above the distributor (cm)
H_0	height of settled bed (cm)
k	constant value for second peak validation
k_b	first order constant for bubble density rate of change ($1/cm^3s$)
$l(x,y)$	pixel luminance in greyscale image
N_b	bubble density ($no./cm^2s$)
N_{b0}	bubble density at the distributor ($no./cm^2s$)
r_b	bubble density rate of change ($no./cm^3s$)
t	thickness of the two-dimensional bed (cm)
Th	threshold value
u	superficial gas velocity (cm/s)
u_b	bubble rise velocity (cm/s)
u_{mf}	minimum fluidization gas velocity (cm/s)
x,y	Cartesian coordinate (cm)
x_c, y_c	bubble centroid coordinates (cm)
X,Y	horizontal and vertical image dimensions in pixel
ΔX_m, ΔY_n	displacement vector (cm)

Greek letters

γ_1,γ_2	gamma distribution coefficients
$\Gamma(m)$	gamma function
ϕ	Davidson's coefficient
Φ	response matrix

making them to rise faster along the bed. The natural phenomena of bubbles break-up and coalescence potentially worsen the scenario. The fluidization quality of a bed is highly dependent on the distribution of bubbles and their physical properties in the bed such as position, dimensions, rise and lateral velocity. The spatial distribution of bubbles is determined by the temporal development of bubbles throughout the fluid bed. Ideally, for there to be good quality fluidization the population of bubbles in the bed should be large but the bubbles should be small in size, homogeneously occupy the bed and have low rise velocities.

To measure bubble parameters, different techniques have been employed which can be broadly classified into two categories, depending on the nature and position of the sensors used: (i) intrusive techniques, namely those based on resistance, inductance, impedance, piezoelectric or thermal probes, and (ii) non-intrusive techniques, among others those based on photographic, X-ray, light scattering and laser techniques.

The use of intrusive techniques implies an intrinsic source of error due to the presence of the measuring tool that creates some level of interference. On the contrary non-intrusive techniques provide good visual observation without interfering with the fluidization process. As an example, Rowe and Partridge [2] purposely developed an X-ray imaging technique to study bubbles in fluidized beds. The technique consisted of penetrating a gas-fluidized bed with X-ray beam to reveal the bubbles within it. Sung and Burgess [3] employed a laser, Glicksman et al. [4] took measurements with optic fibre probes, Atkinson and Clark [5] used pressure probes, while Halow et al. [6] used a high-speed three-dimensional capacitance imaging technique to measure voidage distributions.

In recent years, thanks to the continuous development of digital imaging systems and digital image processing, a great number of researchers have chosen digital visual methods to be applied in the field of experimental fluid dynamics [7–10]. These kinds of techniques play a fundamental role in analysis and data acquisition for multiphase flows such as gas–solid, gas–liquid, solid–liquid flows, where the observation of inter-phase boundaries is relatively simple.

Digital visual methods are limited of course to the case of bi-dimensional fluidized beds, as in this case bubbles can be easily observed.

Caicedo et al. [11] reported an experimental study of bubbling behaviour of gas-fluidized beds using digital image analysis. These authors investigated important parameters of bubbling dynamics such as bubble shape factor and aspect ratio. Experimental runs were conducted at several operation conditions. The results show that the investigated parameters obey to normal distribution across the operating fluid bed, and that statistical analysis must be performed when treating fluidized beds.

Goldschmidt et al. [12] developed an experimental technique based on digital analysis to measure bed expansion and segregation dynamics in dense gas-fluidized beds, in order to validate CFD simulation of mono-disperse and binary mixtures fluid beds. This technique allowed the authors to measure, through the use of differently coloured particles and RGB images decomposition, the extent of mixing and segregation. Extensive data on several systems investigated have been reported.

Shen et al. [13] developed a new method based on image analysis to study the hydrodynamics of two-dimensional bubbling fluidized beds by means of a digital video camera. Simultaneous measurements of size and velocity of gas bubbles were performed, as well as axial and radial distribution of bubble voidage. Equations for bubble diameter and bubble rise velocity prediction for two-dimensional beds were also proposed.

Bokkers et al. [14] studied the extent of mixing and segregation in a bidisperse gas–solid-fluidized bed induced by a single bubble injected in a monodisperse and bidisperse fluidized bed at incipient fluidization and in freely bubbling fluidized beds with both experiments and numerical simulation performed with the Discrete Particle Model. Experiments were run with a pseudo-2D fluidized bed, front-illuminated by halogen lamps. Fluid bed images were taken by means of a high-speed digital camera. The Particle Image Velocimetry (PIV) technique was applied for obtaining particles velocity fields of the experimental runs. The PIV technique adopted is the same widely used for single-

phase fluid flows, with the only exception that fluid seeding is substituted by direct particle tracking.

Cheng et al. [15] used various PIV techniques to investigate the bubbles velocity field in a bidimensional gas–liquid column operated at high bubble density. The authors used the bubbles images of the column recorded by a CCD camera. The images were then post processed off line applying different PIV and PTV (Particle Tracking Velocimetry) cross correlation without any seeding of the fluid, but using bubbles as particles to track. They showed that recursive cross correlation leads to the best measurements results because of the robustness with respect to optical and dynamic characteristic of bubbles.

Zhu et al. [16] reported a study on the characterization of agglomerates in nano-particle fluidization. This study performed size distribution of agglomerates at the bed surface by the use of imaging techniques. Images were recorded by a CCD camera and post processed off line by computer software in order to obtain detailed agglomerates size distribution charts.

Wang et al. [17] used laser-based images to evaluate the size and dimension of aggregates in nano-particles fluidized bed at different inlet gas velocities. To avoid distortion of the aggregate images due to curved surfaces, the authors used a square based fluid bed, instead of circular. The light coming from a pulsed laser was shaped as a sheet and used to illuminate a plane on the fluidized bed, while images were acquired by high resolution CCD camera. The commercial image processing software used allowed the authors to count and measure all aggregates present in each image. Accurate size distribution of aggregates at bed surface were obtained at various operating conditions.

Lim et al. [18] used digital image analysis to investigate bubble distribution and behaviour in planar gas–solid fluidized beds. In this work, frequency domain and statistical analyses of the bed bubble void fraction were used to extensively describe the bed dynamics. Spatial and temporal imaging analyses were used to process image data of the bed and produce visual indication of bubble residence time history patterns for each given state. Frequency and standard deviation of local change in the state of the bed were demonstrated to be useful for inferring the bed fluidization quality.

Many of the above-described research works are based on the use of commercial software to estimate bubble properties. Other works make use of specific manual (i.e. non-automated) steps to perform parts of the calculations. In this work, the focus is on the development of a digital image analysis technique with the specific task of creating a fully automated and robust procedure to purposely measure the most significant bubble properties of two-dimensional bubbling fluidized beds. By in-house development of a suitable software, it is possible to get a total control over every single step of the procedure and every single parameter involved in the calculations, thus achieving a higher level of reliability of the data so far obtained.

Thanks to the high level of automation of the purposely developed procedure it is possible to simultaneously compute a large number of bubble properties, allowing at the same time a meaningful statistical analysis that is intrinsically necessary given the nature of the source data.

2. Experimental

The fluid-bed reactor purposely designed and built for the present investigation is made of Perspex® with dimensions equal to 800 mm (height) × 180 mm (width) × 15 mm (depth). The whole experimental setup is shown in Fig. 1(a).

The reactor is therefore almost two-dimensional, thus allowing visual observations of bubble dynamics within the bed. Glass was used for inner walls to avoid Perspex® surface opacity due to particles attrition phenomena. A plastic porous distributor, whose thickness is equal to 10 mm, is placed at the bottom of the particle bed. Below the distributor a wind box allows to equalize the gas flow.

Air was used as fluidizing gas, whose flow rate was accurately measured through a set of four flowmeters, covering the range 0–140 l/min. A dehumidifier and an oil filter were also mounted on-line on the gas feed.

Glass ballotini were used for all the experimental runs with density equal to 2500 kg/m^3 and diameters in the range 212–250 μm. The particles were filled up to a bed height of 360 mm, referred as H_0. The value of u_{mf} was experimentally determined and found equal to 5.24 cm/s, which soundly coincides with that obtained by Ergun's correlation. Also the value of gas voidage has been experimentally determined and found equal to 0.385, to be compared with the theoretical value assumed equal to 0.4 at minimum fluidization. In these conditions, the fluidized bed had a typical Geldart Group B system behaviour.

In this work, the observation was focused on the whole bed, without selecting any particular region of interest, to allow a full field analysis of the bubbling fluidization dynamics. The flow structure was visualized with the aid of a back-lighting device and recorded by a commercial digital camcorder (Sony, model DCRTRV530E PAL), placed opposite to the bed at a distance of 270 cm, as shown in Fig. 1(b). The use of a CCD camera coupled with an automated computer routine allowed to obtain a significant amount of information, sufficient to perform a statistical analysis via a purposely devised data post-processing.

Continuous high intensity uniform illumination was obtained by placing at the back side of the bed, at approximately 10 cm, six fluorescent lamps, shielded by a flat opaque screen to equalize and diffuse the light. To prevent any shading and direct reflections of the surrounding environment on the Perspex® walls of the bed, the whole set-up was isolated and light-shielded from the external environment by black curtains.

The digital visual acquisition system allowed to collect images of the bed at a frequency of 25 Hz. Each experimental acquisition provides at least 500 frames, equal to 20 s of real time experiment. The presence of a flange that supports the gas distributor avoided visual observation of the lowest 0.8 cm of the bed.

Preliminarily, the measurement device was accurately calibrated by means of a purposely generated set of still images that included horizontal and vertical scales, with rectangular, circular and ellipsoid objects. The calibration procedure consisted of acquiring the set of calibration images by means of the

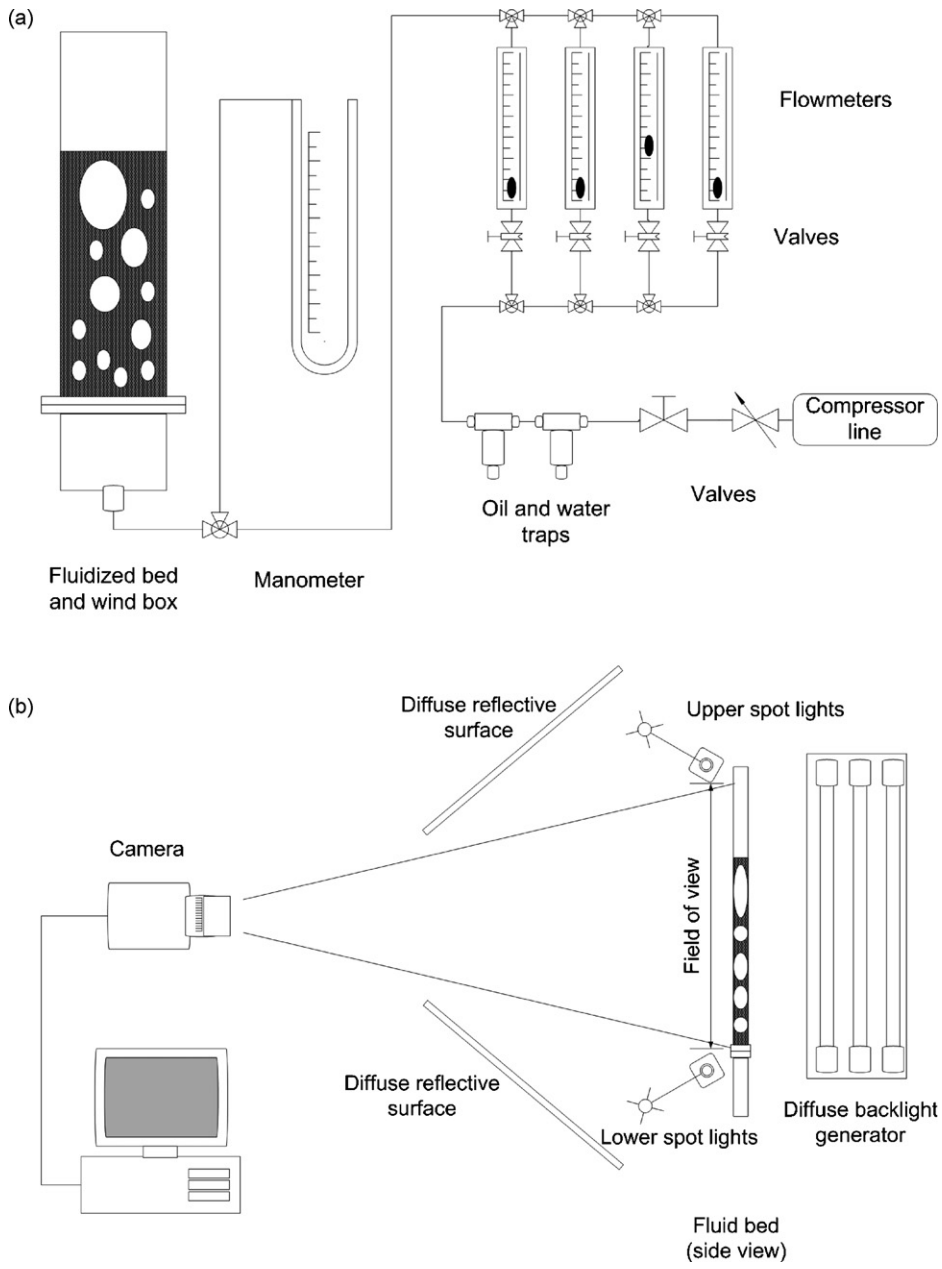

Fig. 1. (a) Experimental set-up (hydraulic scheme) and (b) experimental set-up (optical scheme).

above-described CCD camera, at the same prescribed distance and focal length to be adopted for the whole investigation. Subsequently, the acquired images were processed by means of the automated image analysis routine. As a result, the measurement surface unit was found equal to exactly 1.23×10^{-2} cm^2. As far as the overall distortion of the acquired 720×576 pixel image is concerned, negligible values of vertical and horizontal distortion (i.e. <5%) were found by comparisons with the original physical set of still images used for calibration. Further analysis of error measurements were found equal to 5% of the equivalent diameter for the smallest objects of the calibration images, and equal to 3% for larger objects. The same degree of accuracy has been found for the perimeter measurements, and vertical/horizontal distances.

The image processing routine was developed on Matlab 7.0 (The MathWorks inc.), using the Image Processing Toolbox. Thanks to the flexibility of the Matlab environment almost all steps in image processing, data acquiring and elaboration could be easily automated.

Bubbles in the bed are detected because they create transparent areas in the flat cross-sectional plane of the bed. Thus, light emitted at the back of the bed can pass through and reach the camera. Fig. 2 shows a typical sequence of snapshots of the bubbling fluidized bed, acquired by the above-described system. Black areas represent the emulsion phase of the bed, while white areas are caused by light emitted at the back of the bed passing through the particle-free area, thus highlighting the presence of bubbles.

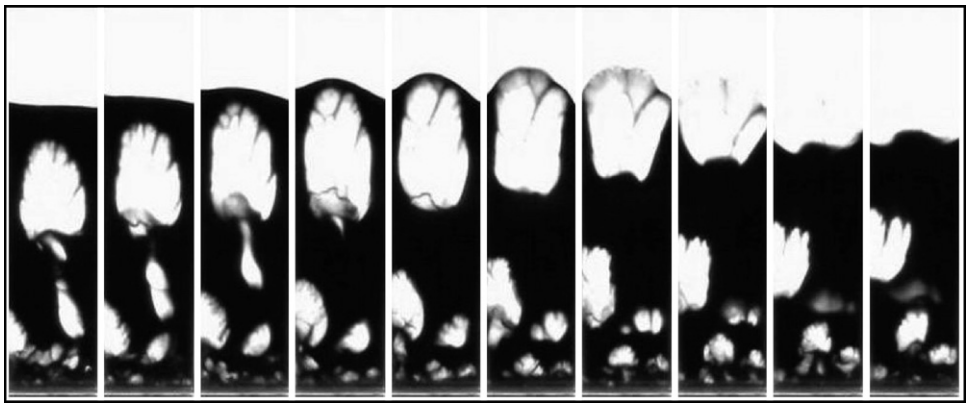

Fig. 2. Snapshot sequence.

3. Digital Image Analysis Technique (DIAT)

The image processing routine is able to collect all data relative to bubbles position, dimension and shape. All frames are automatically analyzed, and data are stored. This allows the off line analysis of a great number of images in reasonable short time.

The routine treats each image individually. Once recalled the image to analyze, the routine works through some simple steps:

(i) Image cropping: the image is cropped to allow the analysis of the fluid bed only, excluding all surroundings from the area of interest;
(ii) Thresholding of the original RGB image to obtain a binary image of the bed. This allows the discrimination of the bubble phase from the dense phase of the bed;
(iii) Indexing of all individual regions inside the area of interest;
(iv) Filtering of false bubbles and peripheral voids;
(v) Property recording of each region inside the area of interest.

Each one of these steps, except the first, requires further discussion which follows below.

The discrimination of the bubble phase from the dense phase is one of the principal difficulties in obtaining quantitative data about bubble dynamics from image analysis. Although there is no complete agreement, Yates et al. [19] suggested a conventional value of 0.80 for voidage fraction of fluid phase as inter-phase boundary for the bubble phase. When high contrast images are available, such as those obtained by the experimental setup shown before, phase identification is made possible by assigning a threshold value to the pixel luminance.

The thresholding procedure can transform a greyscale image (in which any pixel assumes values ranging from 0 to 1) into a binary one, suitable for object identification. This can be accomplished by the following expression, relating the pixel luminance $l(x,y)$ of the original image to the pixel luminance of the binary image $g(x,y)$:

$$g(x, y) = \begin{cases} 1 \Leftrightarrow l(x, y) \geq \mathrm{Th} \\ 0 \Leftrightarrow l(x, y) < \mathrm{Th} \end{cases} \quad (1)$$

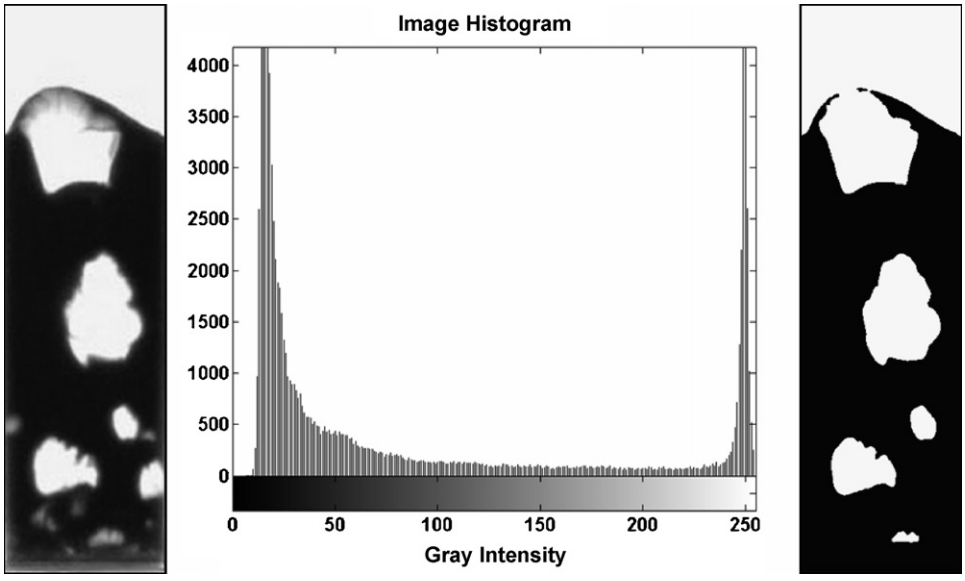

Fig. 3. Original image (left), grey level histogram (centre) and threshold image (right).

All pixels whose luminance value equals 1 are identified as bubble phase pixels, while the others are identified as emulsion or dense phase. One of the crucial steps in image analysis is to choose a proper thresholding value.

The problem is thus converted in finding a correlation between pixel luminance, ranging from 0.0 to 1.0 and voidage, ranging from 0.4 to 1.0. In fact, the conventional distinction between the emulsion phase and the bubble phase is set at a voidage value of 0.80 [19]. If the relation between luminance and voidage were assumed linear, a luminance threshold value of about 0.67 would be used. However, a linear correlation does not hold true in describing the phenomenon of light transmission across a fluid bed, where typically a Beer–Lambert law applies [19–23]. On the other hand, the very wide and flat valley between the peaks in the bimodal distribution of grey level, shown in Fig. 3, ensures that the choice of any arbitrary value of luminance threshold in the range of 0.4–0.8 influences in a marginal way the bubble property measurements. This is equivalent to use the so-called entropy method [24]. The entropy method for thresholding an image is preferable when the two peaks of the grey-level distribution are separated by a wide and flat valley. For the images used in this work, this condition holds true, and the threshold value can be chosen using different considerations.

In the left part of Fig. 3, a typical greyscale bed image is shown, while a typical grey level distribution is shown in the centre of the same figure (it must be noticed that different frames of the same run or different experimental runs give similar histograms).

A value of 0.5 has been carefully chosen by visual observation of binary maps: this value ensures good noise filtration without influencing the measurements.

It must be noted that no image enhancement has been applied in order to fully preserve the original raw data. In Fig. 3 (right), a typical binary image as processed by the Matlab routine is shown.

The binary image thus obtained is then subdivided ("labelled") into different components, based upon connectivity analysis. For each bubble present in the image, its relevant area, equivalent diameter, bubble aspect ratio, that will be defined later, and centroids coordinates are computed. These are recorded in a particular bubble data matrix. Since the aspect ratio of the images is 1:1, distances and areas expressed in pixels can be easily converted in metric distances and areas by multiplying with scale factors.

For each frame, the freeboard is the first region analyzed by the routine. The data relative to the freeboard region, i.e. the freeboard area, are stored in a different matrix from that of bubbles.

Filtering of false bubbles is necessary because of the natural solid recirculation inside each bubble arising in the bed. This phenomenon, in high contrast images appears like a high solid concentration zone at the bottom of the bubble. In the thresholding step, this can lead to the appearance of a bubble followed by a constellation of small bubbles following the first one at the same velocity. The presence of the above mentioned false bubbles and that of peripheral voids, i.e. rising voids adherent to the lateral walls and bubbles bursting at the top of the bed, have been carefully neglected in the statistical analysis of bubble properties.

The two latter steps are automatically done by the Matlab Image Processing Toolbox. It must be noticed that bubbles near the freeboard are considered as individual entities until they burst completely. No extrapolation of the bubble boundary is operated, as done by Shen et al. [13].

After completion of the image analysis and the relevant location of all individual objects in the image, the data have to be processed.

After the thresholding and labelling procedure, geometric properties of all objects (bubbles) found in the image are measured. As already said, data are initially measured in pixel unities and then converted in metric units by using simple scale factors.

Bubble area is calculated as the number of pixels that form each object:

$$A_\mathrm{b} = \sum b(x_j, y_j) = \iint b(x, y)\,\mathrm{d}x\,\mathrm{d}y \tag{2}$$

Bubble centroid coordinates can be computed as follow

$$\begin{aligned} x_\mathrm{c} &= \iint x b(x, y)\,\mathrm{d}x\,\mathrm{d}y/A_\mathrm{b} \\ y_\mathrm{c} &= \iint y b(x, y)\mathrm{d}x\mathrm{d}y/A_\mathrm{b} \end{aligned} \tag{3}$$

where the integrals are extended to the area occupied by the analyzed bubble.

Equivalent diameter is calculated from the knowledge of bubble area:

$$d_\mathrm{b} = \sqrt{\frac{4A_\mathrm{b}}{\pi}} \tag{4}$$

The data obtained can be used to rebuild some important information about the bubble dynamics, such as:

(i) Bed average height as function of time;
(ii) Bubbles hold-up as function of time;
(iii) Distribution of bubble equivalent diameters as function of bubble distance from the distributor;
(iv) Bubble aspect ratio;
(v) Average bubble number as function of the distance from the distributor.

As regards points (iii), (iv) and (v) the statistical analysis was performed by excluding all rising voids adherent to the lateral edges of the bed and those bursting at the top of the bed.

The rising velocity distribution can be found by comparing bubble centroids positions in subsequent frames. Within the present work, two kinds of different velocimetry approaches were developed: (i) Eulerian velocimetry and (ii) Lagrangian velocimetry.

4. Eulerian Velocimetry Technique (EVT)

In this work, a velocimetry procedure based on an Eulerian approach has been applied to measure bubble rise velocities in dense gas–solid fluidized beds. The basic idea of this technique is to correlate the particle position between pairs of subsequent

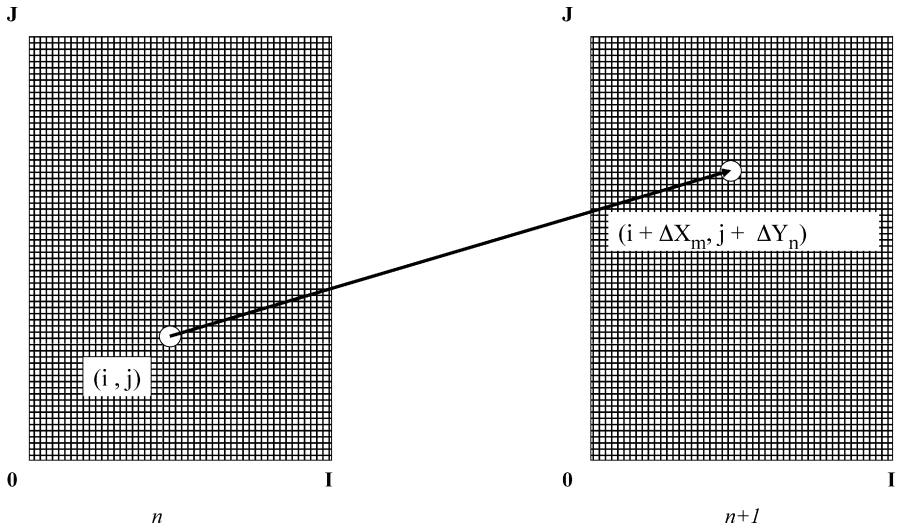

Fig. 4. Cross-correlation computation.

images. For the whole bed area, the most likely displacement vector is found using a cross-correlation analysis technique. The cross-correlation analysis yields a dominant correlation peak embedded in a background of noise peaks, where the location of the tallest peak corresponds to the average bubble displacement. The velocity is then computed from the displacement vector and the time delay between the images. The reliability of this type of velocimetry methodology is based on the assumption that all bubble centroids analyzed have a homogeneous shift between two subsequent frames: this assumption is consistent for bubbles rising in fluidized beds only if their diameter range is narrow enough. The cross correlation between objects, i.e. bubble centroids, in subsequent frames is applied to bubbles of the same diameter class, with a total number of diameter classes chosen equal to 15. In fact, a number of intervals between 10 and 20 give good results. A number of intervals lower than 10 gives a wide distribution of velocities, while numbers higher than 20 give a narrow size distribution and difficulty in finding the same bubble in subsequent frames, due to its natural enlargement.

The procedure is applied to each single bubble diameter class, thus resulting in the computation of an average rising velocity for each single class.

For each single frame, one centroids matrix is created. Such matrix has dimensions XY, where X and Y represents the vertical and lateral dimensions of the bed expressed in terms of number of pixels. In each matrix, the position of all bubble centroids of each bubble diameter class is stored. In particular, all elements of the matrix are zero, except those having a value equal to one corresponding to the location of a bubble centroid.

A global matrix for each given bubble class is finally created by storing each single centroids matrix in a tridimensional matrix whose dimensions are therefore XYF, where F is the total number of frames analyzed.

The cross correlation between two subsequent frames is based on the capability of testing a given displacement vector (ΔX_m, ΔY_n) and evaluating the number of bubble centroids of each given bubble diameter class that exhibit this displacement. This can be accomplished by multiplying the (i, j) element of the general nth centroid matrix with the $(i + \Delta X_m, j + \Delta Y_n)$ element of the subsequent $(n + 1)$th matrix. Since all matrices contain only elements equal to one or zero, the product can be equal to one only if both elements are equal to one. This calculation is repeated for all elements of the nth centroid matrix, thus resulting in the total number of occurrences of that given displacement vector (ΔX_m, ΔY_n).

Subsequently, the procedure is repeated for all the physically acceptable displacement vectors, thus allowing to identify the bubble centroid displacement between two subsequent frames as that particular displacement for which the highest number of occurrences is found.

To formalize this calculation, an individual response matrix Φ is created for each frame couple analyzed. Each element of this response matrix contains the number of occurrences of each given displacement vector so far analyzed. Therefore, each element is computed as in the following, see also Figs. 4 and 5:

$$\Phi(\Delta X_m, \Delta Y_n) = \sum_{\substack{i=1,X \\ j=1,Y}} f_n(i, j) f_{n+1}(i + \Delta X_m, j + \Delta Y_n) \quad (5)$$

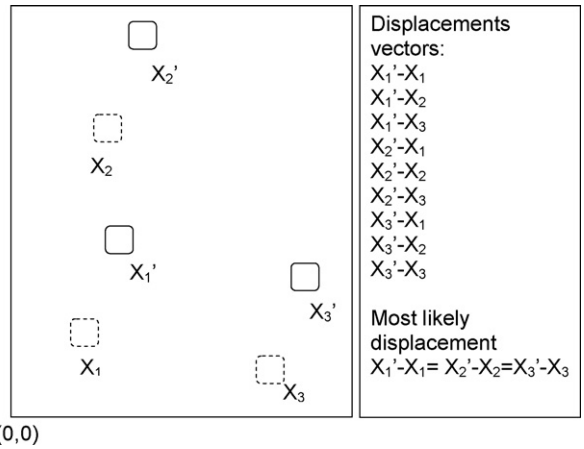

Fig. 5. Eulerian procedure: X_i, centroids positions at time t, X_i', centroids positions at time $t + \mathrm{d}t$.

However, the number of bubbles analyzed for each frame couple is too low to obtain statistically significant velocimetry data. For each bubble, diameter class a global response matrix is therefore computed by simply summing (element by element) all individual response matrices:

$$\Phi_{\text{global}}(\Delta X_m, \Delta Y_n) = \sum_{n=1}^{F-1} \left[\sum_{\substack{i=1,X \\ j=1,Y}} f_n(i, j) f_{n+1}(i + \Delta X_m, j + \Delta Y_n) \right] \quad (6)$$

The primary peak value in the global response matrix allows the recognition of the most likely displacement for all the frame couples analyzed. Secondary peaks are always present, and they are due to false correlations, less likely displacements, bubble nucleation and splitting phenomena, and so on. The global response matrix has the same significance of each response matrix, but it implicitly includes an averaging procedure: hence only very frequent displacements give detectable peaks in the global response matrix. The peak height validation controls the goodness of the cross-correlation, by comparing the highest peak with the second highest peak:

$$\frac{\text{Highest peak}}{\text{Second highest peak}} \geq k \quad (7)$$

with k in the range 1.0–1.5.

It is worth noting that the procedure is able to compute average bubble rise velocities for each bubble diameter class. It must be noted that the detectable bubble centroid displacement is intrinsically discrete, since the minimum detectable displacement between two subsequent frames is equal to the size of one image pixel. This can lead to poorness of data for slowly moving bubbles, whose displacement is of the order of a few pixels, and it can be solved by using high-definition cameras coupled with appropriate image acquisition rates.

By this procedure, the bubble velocity distribution as function of bubble diameter can be found. In this distribution, a number of points at least equal to the number of diameter intervals is obtained. If some points do not satisfy the second peak validation, they are not presented in any way.

5. Lagrangian Velocimetry Technique (LVT)

The Lagrangian velocimetry technique (LVT) uses a different way of computing the displacement of each bubble in subsequent frames. This procedure is able to assign to each bubble a unique number, and thus it is able to follow each bubble in different frames. Differently from Eulerian velocimetry (EVT), it is possible to follow each bubble in its evolution from the formation to coalescence with another bubble or bursting at the freeboard.

The algorithm consists of the following steps:

(i) All bubbles present in the first frame are sequentially numbered. This is automatically done by the processing routine. All bubbles present in the second frame are initially not numbered;
(ii) For a given bubble in the first frame, the procedure will locate the bubble present in the subsequent frame exhibiting a displacement physically consistent. This is done by finding in the subsequent frame; all bubbles with a rise velocity greater than zero but lower than the maximum expected velocity, and a lateral velocity with absolute value lower than the maximum expected lateral velocity. To this bubble, the same number of the bubble present in the first frame is assigned. If more than one bubble, present in the second frame, exhibits a physically consistent displacement with respect to the bubble considered in the first frame, then the same number of the bubble present in the first frame is assigned to the bubble of the second frame having minimum distance from bubble of the first frame;
(iii) Repeat step (ii) for all bubbles in frame 1;
(iv) Assign, to all bubbles in frame 2 still not having a number, a new unique number: this is equivalent to consider these bubbles as new ones;
(v) Repeat the procedure for all frames.

Once all bubbles have been indexed, the data processing starts with the filtering of bubbles that appear for less than a threshold number of frames, typically set to 3. This allows the exclusion of not statistically significant tracked bubbles. For each bubble, accurate velocity measurement is possible, by simply evaluating the displacement of its centroid between subsequent frames. For a generic bubble, indexed with subscript i, that appears in two subsequent frames, labelled with subscript n and $n+1$, respectively, the displacement is computed as the difference of the bubble centroid coordinates in the two frames $(\Delta X, \Delta Y) = (x_{i,n+1} - x_{i,n}, y_{i,n+1} - y_{i,n})$.

By adopting the LVT procedure, it is finally possible to obtain:

(i) Distribution (cloud) of bubble rise velocities and average velocity as function of equivalent diameter;
(ii) Distribution (cloud) of bubble lateral velocities as function of equivalent diameter;
(iii) Distribution of bubble rise angle (probability plot);
(iv) Statistical distribution of velocity coefficients ϕ for each bubble, where the bubble velocity is given by $u_b = \phi (g d_b)^{0.5}$.

Once the bubbles rising up through the bed are indexed as above described, it is possible to measure other bubble local properties and follow the time evolution of each property for each bubble through its path along the bed.

6. Discussion on DIAT results

As previously mentioned, for the purpose of the present work all results refer only to the case of glass ballotini, having density equal to 2500 kg/m^3 and diameter in the range 212–250 μm, fluidized with air at a superficial gas velocity of $3.4u_{mf}$.

The application of the presently proposed DIAT to the sequence of frames recorded during the experimental run by the digital camcorder resulted into the following data: bubble diameter distributions, bubble aspect ratio distribution, bub-

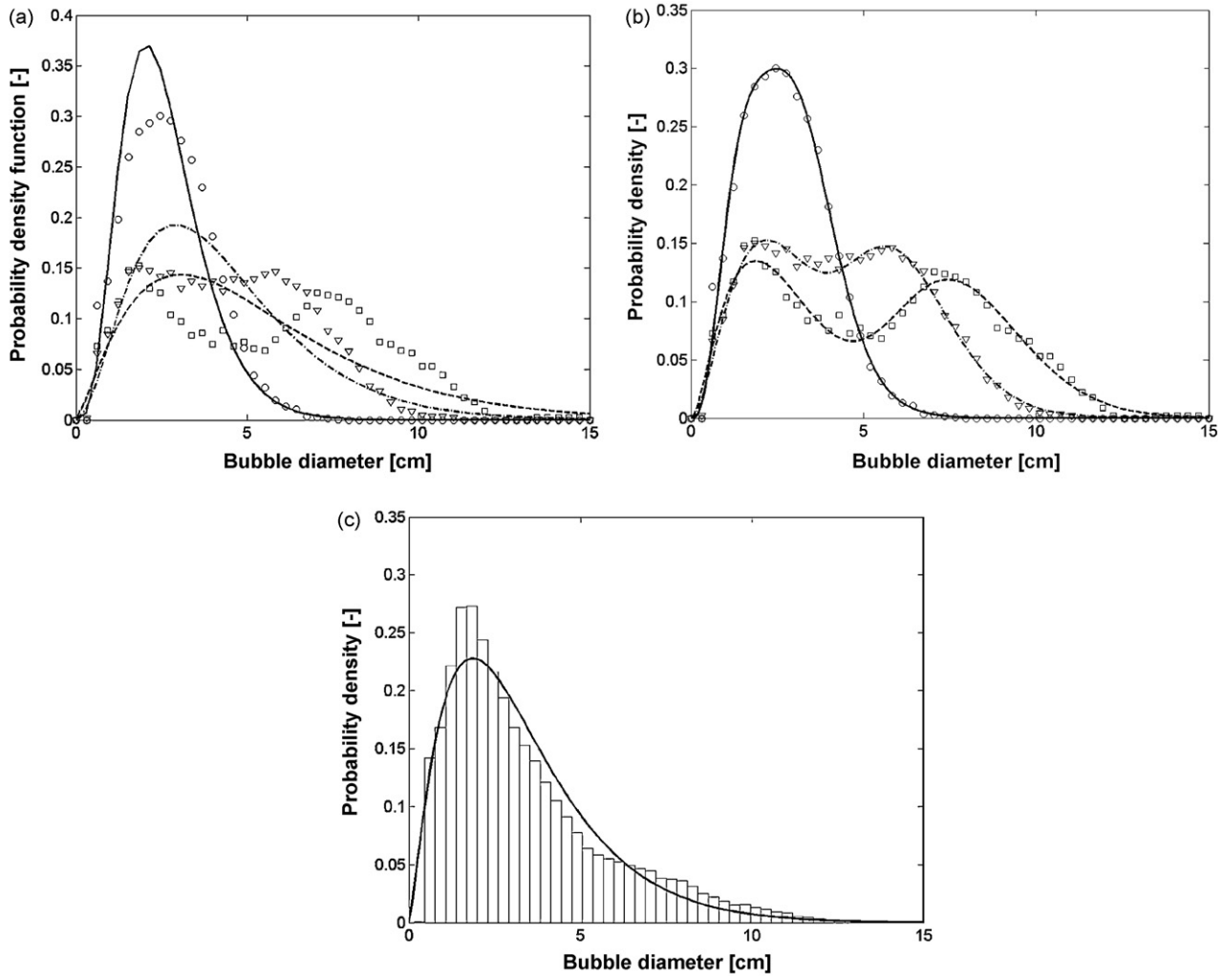

Fig. 6. (a) Bubble size distribution at different bed heights and relevant gamma distribution fittings: Symbols, experimental data. Lines, gamma fit. Solid line and circles, $H = 0.25H_0$. Dotted line and triangles, $H = 0.5H_0$, dash-dot line and squares, $H = 0.75H_0$. (b) Bubble size distribution at different bed heights and relevant bimodal gamma distribution fittings: symbols, experimental data. Lines, gamma fit. Solid line and circles, $H = 0.25H_0$. Dash-dot lines and triangles, $H = 0.5H_0$, dashed line and squares, $H = 0.75H_0$. (c) Overall statistical distribution of bubble diameters and relevant fit with gamma distribution.

ble density distribution, bed expansion and bubble hold-up dynamics.

Fig. 6(a) reports the experimental bubble equivalent diameter distributions recorded in three different slices of the bed, whose baricentral elevations are $0.25H_0$, $0.50H_0$, $0.75H_0$, respectively. It can be easily observed that, for the case of lower elevation (i.e. $0.25H_0$), the experimental data show a skewed distribution with one single peak. This finding may be explained by taking into account that at all elevations near the distributor the prevalent phenomenon is the growth of almost mono-sized bubbles, with negligible break-up and coalescence. At higher elevations (i.e. $0.50H_0$ and $0.75H_0$), the dynamic behaviour of bubbles is more complex, since there is the simultaneous presence of bubble growth and nucleation, bubble break-up and coalescence phenomena. The effects of the latter phenomena increase with elevation, resulting into the data distribution to change progressively from a skewed monomodal distribution into a skewed bimodal distribution.

As a matter of fact, there is evidence in the literature [25] that the description of the bubble size distribution at any given elevation can be accomplished by a choice of distribution functions. Typical choices are (i) log-normal or (ii) gamma distributions. For the latter, the mathematical formulation is reported below:

$$p\,\mathrm{d}f(d_\mathrm{b}|\gamma_1,\gamma_2) = \frac{1}{\gamma_2^{\gamma_1}\Gamma(\gamma_1)} d_\mathrm{b}^{\gamma_1-1}\,\mathrm{e}^{-d_\mathrm{b}/\gamma_2} \tag{8}$$

$$\Gamma(m) = \int_0^\infty x^{m-1}\,\mathrm{e}^{-x}\,\mathrm{d}x \tag{9}$$

In Fig. 6(a), the experimental data are also fitted by relevant Gamma distributions whose parameters are computed by using the maximum likelihood method. It can be easily observed that, as expected, the fitting works fairly only for the case of lower elevation, while at higher elevations the previously mentioned

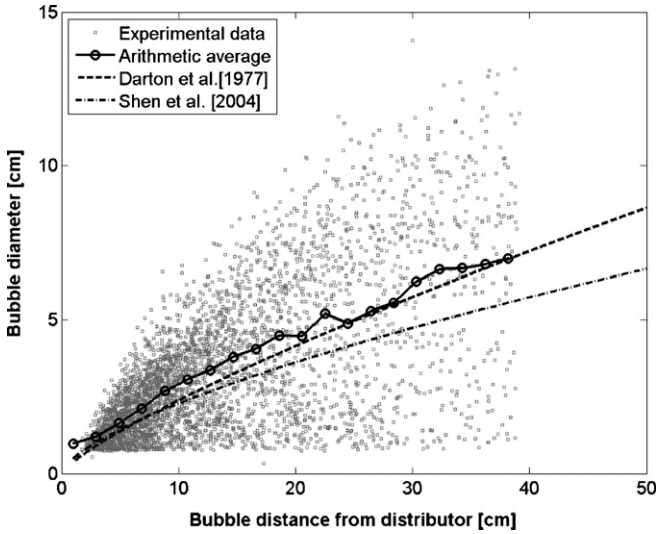

Fig. 7. Bubble diameter distribution as function of bubble distance from distributor, with arithmetic and area-weighted mean curves.

complex bubble dynamic behaviour does require a more complex mathematical description.

This is accomplished by a purposely weighed linear combination of two Gamma distributions, the results of such fitting is reported in Fig. 6(b), where a smooth agreement with experimental data can be observed.

The overall statistical distribution of bubble diameters in the whole bed is finally reported in Fig. 6(c). Again, the distribution appears clearly skewed, but the bimodal distribution observed in Fig. 6(b) now appears to be dumped. Fitting by a gamma function reveals an acceptable agreement between the data and the chosen distribution.

In Fig. 7, the bubble equivalent diameter distribution is reported as a function of the distance of the bubble centroid from the distributor. Although the data assume the form of a wide cloud, mainly because of the chaotic behaviour of the bubbling bed, a trend in bubble growth is evident. This can be suitably highlighted by plotting the bubble average diameter distribution. This is computed by dividing the maximum measured bubble height above the distributor in a fixed number of intervals, selecting all bubbles in each interval and computing the average diameter. Thus, a number of average diameters, equal to the number of intervals selected (20 in this work) to discretize the bubble distance from the distributor, was obtained. Fig. 7 shows the average diameter trend, plotted together with those computed by two correlations proposed by Darton et al. [26] and Shen et al. [13], respectively.

In particular, Darton et al. [26] studied the bubble growth phenomenon and concluded that bubbles coalescence in fluidized beds leads to the increase of bubble size with distance from the distributor. The phenomenon is described by an equation for the bubble diameter:

$$d_b = \frac{0.54(u - u_{mf})^{0.4}(h + 4\sqrt{A_0})^{0.8}}{g^{0.2}} \quad (10)$$

where d_b is the diameter of the sphere having the same volume as the bubble, u the superficial gas velocity, u_{mf} the superficial gas velocity at incipient fluidization, h the height above the distributor, g the acceleration due to gravity, and A_0 is usually the area of the distributor per orifice.

The basis of the theory is that bubbles tend to rise in preferred paths and that the distance travelled by two neighbouring bubbles before coalescence is proportional to their lateral separation. With the empirical constant 0.54, the above equation agrees quite well with most literature data on bubble size, provided that bubble growth is not limited by the presence of fine particles.

More recently, Shen et al. [13] proposed an equation to predict bubble diameter for the case of two-dimensional beds. The form of the equation is similar to that of Darton et al. [26] and is reported below:

$$d_b = \frac{0.89[(u - u_{mf})(h + 3.0A_0/t)]^{2/3}}{g^{1/3}} \quad (11)$$

where t is the thickness of the two-dimensional bed.

In absence of available data on the distributor characteristics, both Darton et al. [26] and Shen et al. [13] suggested a value for A_0 equal to zero.

By comparing the experimental trend of bubble average diameter with the predictions obtained by the correlation of Darton et al. [26] a fair agreement is found. The correlation by Shen et al. [13] appears to noticeably underestimate the observed bubble growth along bed height.

A further step in the analysis of bubble properties concerns the shape and its evolution along bed height. In Fig. 8(a), the overall distribution of bubble aspect ratio is reported. In the present work, the aspect ratio is actually defined as the ratio between the bubble maximum horizontal extension and its maximum vertical extension.

It is worth pointing out that the typical mushroom shape observed for bubbles in bubbling beds is due to the presence of a wake region at the bottom. Thus, a vertically oblong ellipsoidal bubble would exhibit in most cases a maximum vertical extension at least equal or even greater than its horizontal maximum extension, resulting in typical aspect ratio values lower than 1.0. Conversely, a horizontally oblong ellipsoidal bubble would exhibit a maximum vertical extension smaller than its horizontal maximum extension, thus resulting in aspect ratio values greater than 1.0.

As it can be readily observed in Fig. 8(a), the distribution is positively skewed and presents a mode in the range where the bubble aspect ratio is equal to 1.0. A possible explanation for such positive skewness is to be found in a significant number of bubbles of small-to-medium size, whose typical shape is horizontally oblong. However, the finding that the value of the mode is practically equal to 1.0 indicates that a predominantly large number of bubbles are slightly vertically oblong.

A confirming evidence is given in Fig. 8(b), where the distribution of bubble aspect ratio is reported for three different elevations along the bed height. Interestingly, the value of the mode is progressively shifted towards the left hand side when moving from the bottom to the top of the bed, thus highlight-

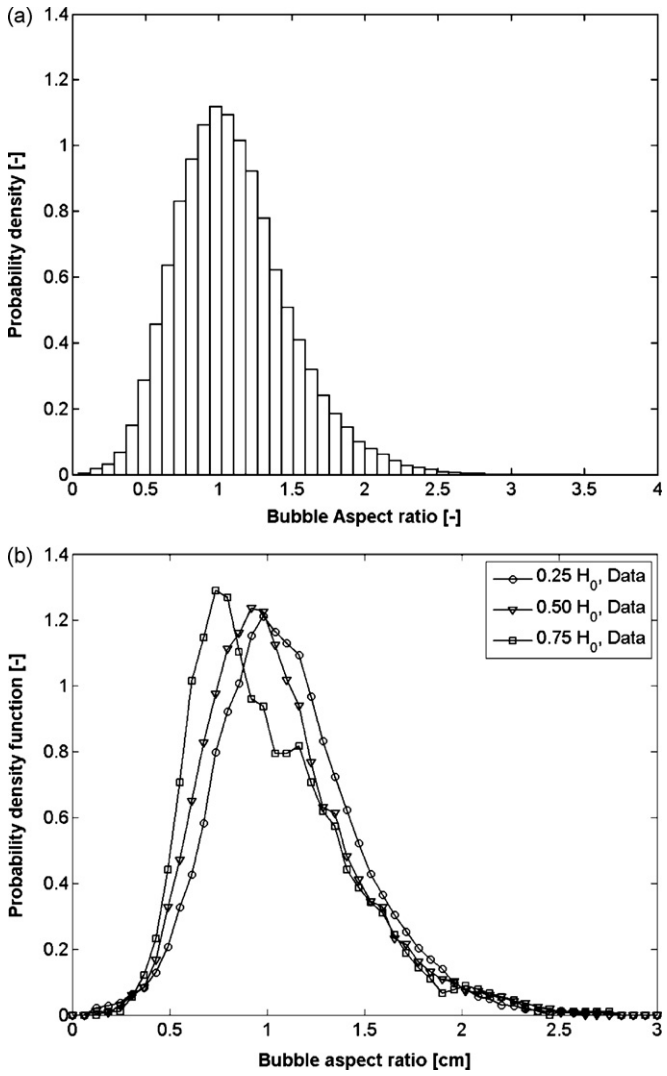

Fig. 8. (a) Distribution of bubble aspect ratio. (b) Distribution of bubble aspect ratio.

ing the dynamic of the bubble shape along bed height. In other words, it is evident that at lower elevations bubbles are still to grow and therefore exhibit a shape closest to spherical; conversely at higher elevations bubble growth leads to vertically oblong shapes, whose elongation is more and more pronounced with increasing elevation. At all elevations, it should be observed that the presence of the tail in the positive skewed distributions indicates the presence of small-to-medium size horizontally oblong bubbles.

Fig. 9 shows the average bubble density along the bed height. The bubble density is computed by discretizing the whole bed height in a certain number of slices, 20 in this work, and calculating the number of bubble centroids falling into each slice. This procedure is repeated for each individual frame and the results are averaged over all the 500 frames analyzed.

A linear decay of bubble density can be easily observed in the semi-logarithmic chart of Fig. 9. Such a behaviour for a bubbling bed can be explained by performing a simple bubble density balance over an infinitesimal section of the bed, which

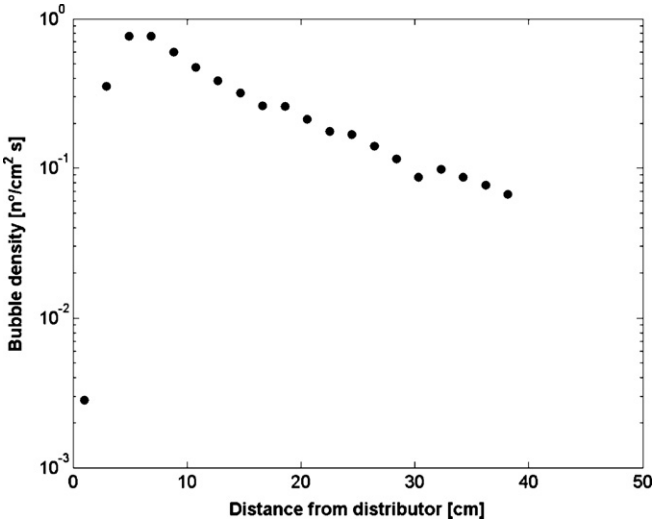

Fig. 9. Distribution of bubble density along bed height.

gives:

$$N_b|_{z+dz} = N_b|_z + r_b\,dz \tag{12}$$

where r_b is the bubble density rate of change per unit volume of bed. Rearranging

$$\frac{dN_b}{dz} = r_b \tag{13}$$

Assuming that the bubble density rate of change per unit volume of bed is proportional to bubble density itself (first order decay rate)

$$\frac{dN_b}{dz} = k_b N_b \tag{14}$$

and integrating

$$\ln\left(\frac{N_b}{N_{b,0}}\right) = k_b h \tag{15}$$

one finally gets

$$\ln N_b = k_b h + \ln N_{b,0} \tag{16}$$

which is in fact a first-order bubble coalescence rate. Conversely, a constant value of bubble density would be typical of fully developed slug flows.

Fig. 10 reports the instantaneous dimensionless bed height as function of time. The bed height dynamic is computed by measuring the area of the freeboard region of each single frame analyzed, dividing it by the bed width and subtracting the obtained value from the total height of the reactor. The observed dynamic of bed height fluctuations is that typical of a freely bubbling bed, with peaks due to the splash of bubbles reaching the freeboard region.

Fig. 11(a) reports the global bubble hold-up dynamics. This is computed by summing, for each frame, all bubble areas and dividing it by the whole bed area. Again, the observed dynamic of the global bubble hold-up is that typical of a freely bubbling bed, with the amplitude of the fluctuations essentially due to bubble bursting. It must be noted that the bed expansion dynamic

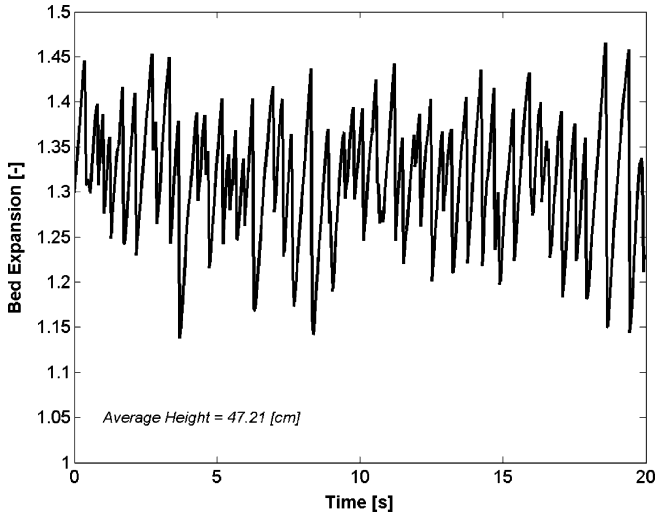

Fig. 10. Instantaneous bed height.

reported in Fig. 10 and the bubble hold-up dynamic shown in Fig. 11(a) are somewhat different. The former is a global parameter influenced by the extent of the bubble phase together with the expansion of the emulsion phase, the latter measures just bubbles overall content. From the knowledge of both measurements, it would then be possible to estimate the overall expansion of the emulsion phase (including interstitial expansion and the so-called cloud region around bubbles).

Fig. 11(b) shows the time averaged local bubble hold-up distribution map. This is computed on the basis of the definition of bubble hold-up over any control volume of the bed:

$$\text{Holdup}_{\substack{\text{global}\\\text{inst}}} = \frac{\int_V V_{\text{bubbles}}\,\mathrm{d}V}{\int_V V_{\text{emulsion}}\,\mathrm{d}V + \int_V V_{\text{bubbles}}\,\mathrm{d}V} \tag{17}$$

If the control volume is infinitesimal, it cannot admit the contemporary presence of both phases, thus the local bubble hold-up can be replaced with an instantaneous phase indicator:

$$G(x,y) = \lim_{V\to 0} \frac{\int_V V_{\text{bubbles}}\,\mathrm{d}V}{V} = \begin{cases} 1 \text{ if } G \in \text{bubble phase} \\ 0 \text{ if } G \in \text{emulsion phase} \end{cases} \tag{18}$$

This definition of phase indicator is immediately applicable to compute local time-averaged values of bubble hold-up by means of DIAT, since function $G(x,y)$ exactly coincides with the instantaneous pixel luminance value computed for each thresholded binary image analyzed by DIAT (as previously described in the relevant paragraph). Local time-averaged bubble hold-up values are therefore given by the following expression:

$$\text{Holdup}_{\substack{\text{local}\\\text{avg}}} = \frac{1}{T}\int_T G(x,y)\,\mathrm{d}t = \frac{1}{T}\int_T g(x,y)\,\mathrm{d}t \tag{19}$$

It is thus possible to produce the time-averaged bubble hold-up distribution map reported in Fig. 11(b) by simply repeating the computation of Eq. (19) over the entire bed domain.

The analysis of time averaged bubble phase hold-up allows the visual observation of preferential bubble paths along the bed, with a reverse-Y shaped pattern starting near the bed bottom and developing in the upper regions of the bed. The reverse-Y shaped pattern is due to the coalescence-driven bubble dynamics prevailing after bubble nucleation in the proximity of the distributor in the intermediate region of the bed, resulting in the formation of a single central preferential path in the upper regions of the bed if the bed height is sufficient [18].

7. Discussion on EVT and LVT results

The data reported so far in Figs. 6–11 were obtained on the sole basis of the DIAT without the need of any velocimetry

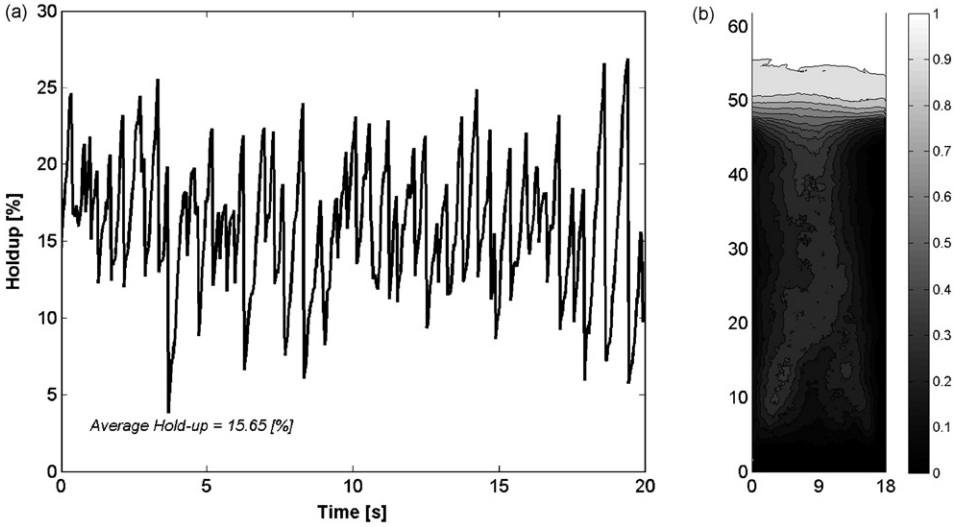

Fig. 11. (a) Bubble global hold-up. (b) Time-averaged bubble local hold-up.

technique. In the following series of figures, the data obtained via EVT and LVT are reported.

In particular, typical velocimetry data obtained by EVT are shown in Fig. 12, while additional results obtained by LVT are shown in the figures from 13 to 19.

In Fig. 12, the bubble rise velocity computed by EVT as a function of bubble diameter is reported. As mentioned earlier, the bubble rise velocities are computed directly via the cross correlation procedure that computes the average rising velocity of each selected bubble diameter interval. Thus, a number of average rising velocity points equal to no more than the number of bubble diameter intervals selected for the cross correlation procedure is plotted.

The data reported in Fig. 12 show, as expected, a general tendency for bubble rise velocities to increase with bubble diameter. However, two different trends appear to exist. In particular, at smaller bubble diameters, the rise velocities appear to increase more slowly, while at larger bubble diameters the rise velocities appear to increase more rapidly. Obviously an intermediate bubble diameter interval can be easily located where this change of behaviour occurs.

In the same graph, two correlations available in literature, i.e. Davidson and Harrison [27], Shen et al. [13] are plotted. Both correlations have the same functional form

$$u_b = \phi(g d_b)^{0.5} \tag{20}$$

Davidson and Harrison [27] propose a value for the velocity coefficient of $\phi \approx 0.71$, whereas Shen et al. [13] propose $\phi \approx 0.8$–1, specifically measured for 2D fluidized beds. As it can easily be seen, the prediction of both literature correlations appear to significantly overestimate the bubbles rise velocity distribution.

Starting with LVT analysis, Fig. 13 reports the vertical position of the tracked bubbles as a function of time. This allows a visual observation of the tracking procedure robustness and reliability, proven by the smooth behaviour of the measured trajectories.

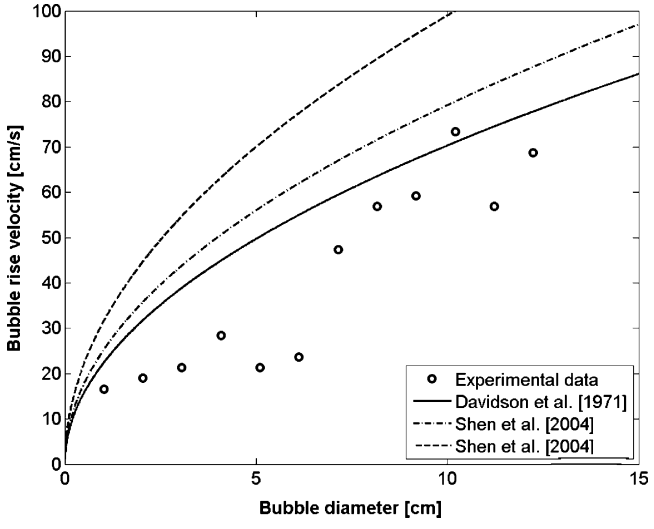

Fig. 12. Bubble rise velocity distribution as computed by the Eulerian procedure. Solid line $\Phi = 0.71$, dashed line $\Phi = 0.80$ and dashed dot line $\Phi = 1.0$.

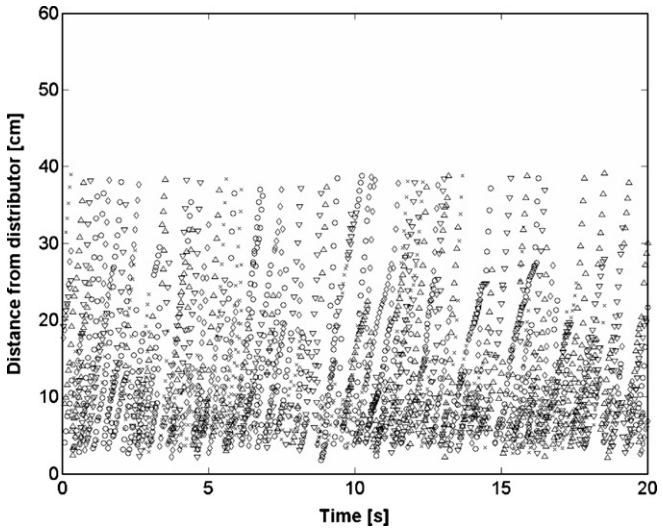

Fig. 13. Bubble vertical trajectories computed via Lagrangian tracking.

Fig. 14(a) shows the bubble rise velocities distribution as computed by means of LVT and its relevant averaged-data curve. As for the case of EVT reported in Fig. 12, a general tendency for bubble rise velocities to increase with bubble diameter is observed. The data appears evidently widely scattered resulting in a cloud, as a result of the complex interactions due to bubble nucleation and growth, bubble break-up and coalescence dynamics along the bed height. Interestingly averaged-data obtained by LVT exhibit a smooth trend, clearly indicating the bubble rise velocities increase with bubble diameter.

In the same graph, the bubble rise velocity curve computed by the correlations of Davidson and Harrison [27] is plotted. Again, the velocities predictions obtained by the literature correlation proposed appear to overestimate the measured rise velocities distribution.

In the same figure, a comparison of the LVT averaged-data with the corresponding EVT averaged-data results in a marked difference in the region of smaller diameters. Conversely, the velocimetry data obtained by EVT and LVT are in smooth agreement for greater bubbles. Of course an explanation for this occurrence must be found in the different computational approaches at the base of the EVT and LVT, respectively. In fact, the EVT procedure reveals the most probable displacement, i.e. the mode of the rise velocity distribution for each diameter class. Thus, the averaged-data curve by LVT should produce almost the same data obtained by EVT provided that the distribution of velocity for any considered diameter class is symmetrical. Conversely, if the distribution of velocity for any considered diameter class is skewed then a different value would be computed by EVT and LVT, respectively. In fact in Fig. 14(b), the averaged-data LVT curve has been substituted by the corresponding curve of the modes of the LVT velocity distributions for each diameter class; the reported curve exhibits now a better agreement with EVT measurements. Moreover, the analysis of Fig. 14(a) and (b) highlights a characteristic positive skewness of velocity measurements for the range of smaller diameters.

Fig. 15 shows the distribution of the velocity coefficient, ϕ, as defined in Eq. (20). This is computed for each bubble by data

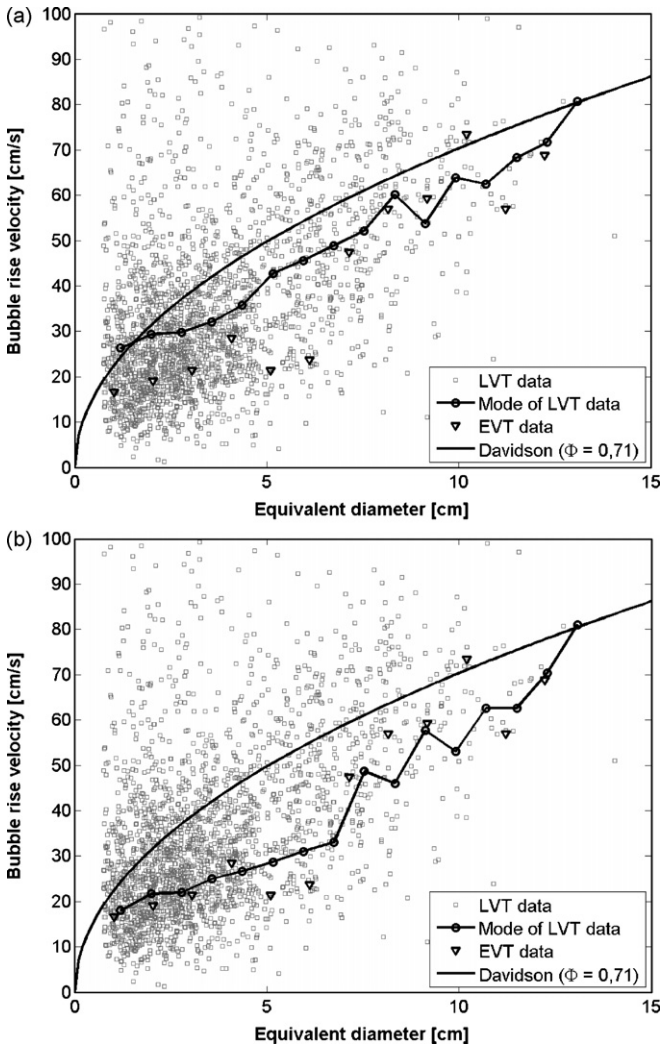

Fig. 14. (a) Bubble rise velocity distribution as computed via Lagrangian tracking, compared with relevant average curve and EVT measure. (b) Bubble rise velocity distribution as computed via Lagrangian tracking, compared with relevant modes curve and EVT measure.

fitting. The observed statistical distribution of data is skewed, with a value of the mode in the range 0.5–0.6 and a mean of 0.63. The skewed distribution of the velocity coefficients noticeably descends from the overall skewed distribution of bubble diameters shown in Fig. 6(c). As a consequence of the use of Gamma functions to describe the statistical distribution of bubble diameters, the Gamma distribution that best fits the data on velocity coefficients has been computed with the method of maximum likelihood. The resulting curve is in good agreement with the data.

Fig. 16 shows bubble lateral velocity as measured with LVT versus the equivalent diameter. In the same figure, a linear regression of the data is plotted (solid black line), showing the absence of any trend, as expected. Moreover, it can be observed that smaller bubbles exhibit generally more pronounced lateral displacements in accordance to the coalescence mechanism of bubbles in freely bubbling fluidized beds. This mechanism in fact involves a "lateral capture" of smaller bubbles, as reported by Darton et al. [26], whereas greater bubbles, to be preferentially

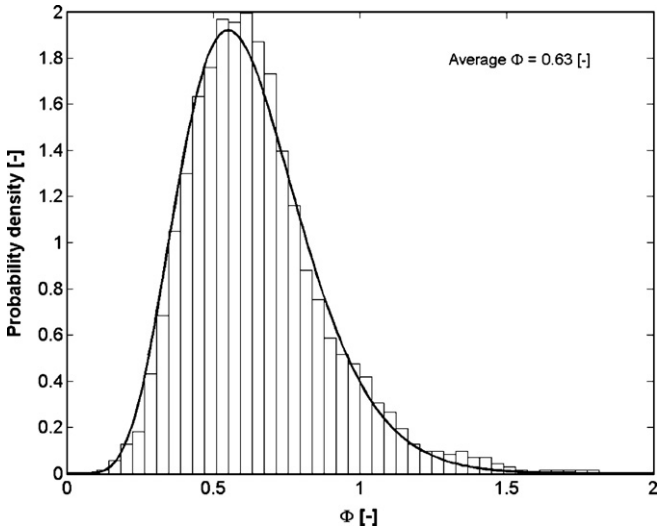

Fig. 15. Davidson's coefficient distribution and relevant gamma distribution fit.

found in the upper regions of the bed, tend to rise undisturbed towards the bed surface.

Fig. 17 reports the distribution of the rising angle of bubbles. The rising angle is simply computed from knowledge of the local velocity components for each bubble. Thus, a distribution of rising angles can be obtained. Accordingly with the random nature of the lateral displacements of the bubbles and with the symmetry of the system investigated, a normal distribution has been chosen to fit the data. The normal distribution that best fits the rising angle distribution has been computed again by the maximum likelihood method, and it is shown in the same figure. The slight symmetrical disagreement found between data and the proposed normal distribution probably will require further investigations.

In Fig. 18, the velocity components distribution is reported, in the form of a grey-scale contour plot. It allows the simultaneous visualization of the following quantities: (i) skewness of the rise velocity distribution; (ii) symmetry of lateral veloci-

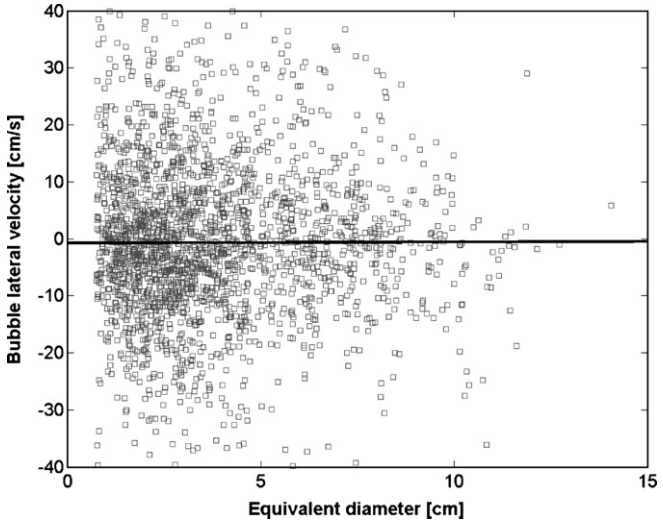

Fig. 16. Bubble lateral velocity distribution as computed via Lagrangian tracking.

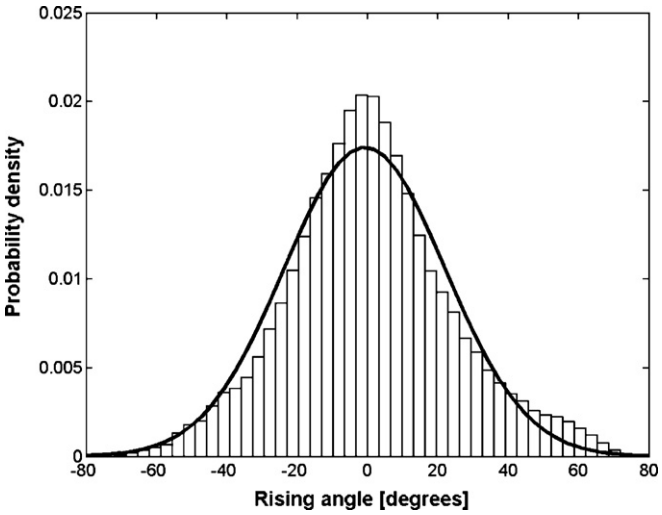

Fig. 17. Bubble rising angle distribution and normal distribution fit.

ties distribution. Moreover, this kind of plot allows to check the correctness of the maximum rise and lateral velocities used in the LVT procedure: if the limiting velocities were too small with respect to the actual velocities, then the contour plot of Fig. 18 would present velocity contour levels significantly greater than zero all along the boundary of the bed. On the contrary, the choice of very high values of limiting velocities, with respect to the actual ones, could result in a too high level of noise in the distribution due to increased errors in the tracking procedure.

Finally in Fig. 19, a time-averaged vector plot of bubbles velocity is depicted. As physically expected, bubble trajectories are slightly oriented towards the centre of the bed in the lower part of the bed and then directed vertically in the upper section of the bed. Fig. 19 gives confirming complementary information to that previously shown in the local hold-up map of Fig. 11(b). This latter allows the visualization of the preferential bubble paths along the bed height, whereas the former associates the relevant bubble average velocity to preferential paths.

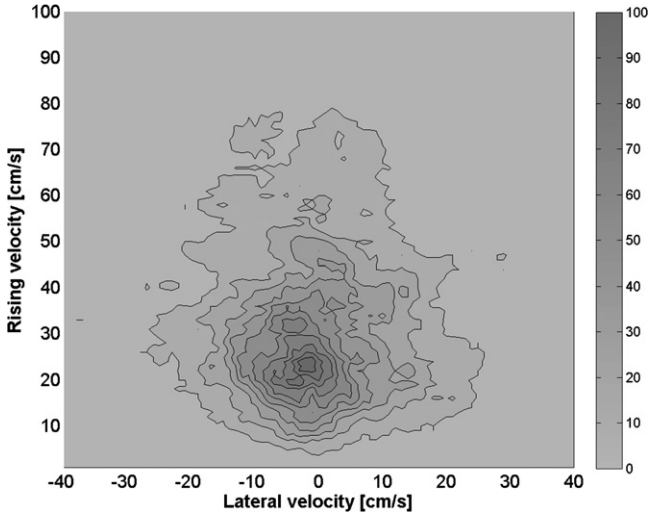

Fig. 18. Velocity components contour plot.

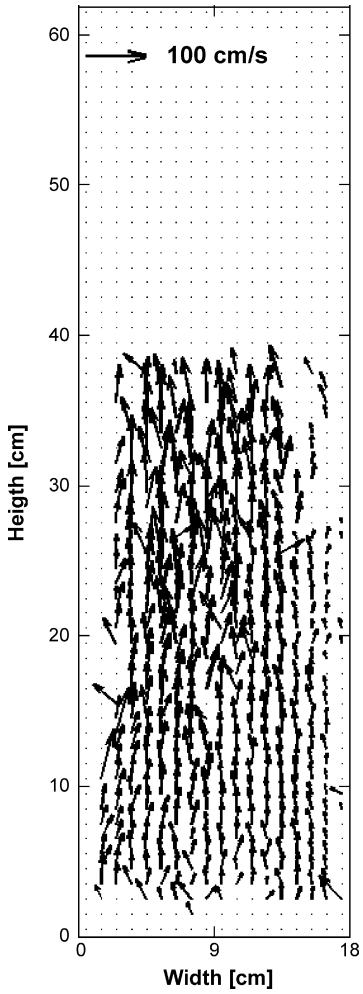

Fig. 19. Time-averaged bubble vector plot.

8. Conclusions

A digital image analysis technique (DIAT) was developed in this work to study the hydrodynamics of a lab-scale two-dimensional bubbling fluidized bed. The DIAT allows for the simultaneous measurements of the most significant bubble properties by means of a purposely in-house developed software. Two kinds of velocimetry techniques have been developed in order to self-validate velocity measurements: (i) an Eulerian velocimetry technique (EVT), based on a suitable cross correlation between subsequent frames, and (ii) a Lagrangian velocimetry technique (LVT), consisting of a bubble tracking to specifically follow bubble evolution along the bed.

The statistical analysis performed on the test case here presented allows to state that the highly automated technique here developed may well be used to fully characterize the complex dynamic behaviour of freely bubbling beds, highlighting its large potential.

Moreover, the present image analysis technique may well be applied, as a post-processing tool particularly useful for validation, also to the case of CFD simulations of bubbling fluidized beds where results may be conveniently shown in terms of solid (or gas) phase distribution maps. This will be fully addressed in a paper to follow.

Acknowledgements

In loving memory of Luca Cammarata whose promising research efforts into the field of fluidization were so prematurely forced to end.

This work was carried out within the framework of the PRIN 2005 research program "Study of fluidized beds stabilized by means of electric or magnetic fields" funded by the Italian Ministry of University.

References

[1] F. Johnsson, S. Andersson, B. Leckner, Expansion of a freely bubbling fluidized bed, Powder Technol. 68 (2) (1991) 117–123.
[2] P.N. Rowe, B.A. Partridge, An X-ray study of bubbles in fluidized beds, Trans. Instn. Chem. Engrs. 43 (1965) 157–175.
[3] J.S. Sung, J.M. Burgess, A laser based method for bubble parameter measurement in two dimensional-fluidized beds, Powder Technol. 49 (1987) 165–175.
[4] L.R. Glicksman, W.K. Lord, M. Sakagami, Bubble properties in large particle fluidized beds, Chem. Eng. Sci. 42 (1987) 479–491.
[5] C.M. Atkinson, N.N. Clark, Gas sampling from fluidized beds. A novel probe system, Powder Technol. 54 (1988) 59–70.
[6] J.S. Halow, G.E. Fasching, P. Nicoletti, J.L. Spenik, Observation of a fluidized bed using capacitance imaging, Chem. Eng. Sci. 48 (1993) 643–659.
[7] P.K. Agarwal, Bubble characteristics in gas-fluidized beds, Chem. Eng. Res. Des. 63 (1985) 323–337.
[8] K.S. Lim, P.K. Agarwal, Conversion of pierced lengths measured at a probe to bubble size measures: an assessment of the geometrical probability approach and bubble shape models, Power Technol. 63 (1990) 205–219.
[9] D. Gera, M. Gautam, Bubble rise velocity in two-dimensional fluidized beds, Powder Technol. 84 (1995) 283–285.
[10] A.S. Hull, Z. Chem, J.W. Fritz, P.K. Agarwal, Influence of horizontal tube tanks on the behaviour of bubbling fluidized beds. 1. Bubble hydrodynamics, Powder Technol. 103 (1999) 230–242.
[11] G.R. Caicedo, J.J. Prieto Marqués, M. Garcia Ruis, J. Guardiola Soler, A study on the behaviour of bubbles of a 2D gas–solid fluidized bed using digital image analysis, Chem. Eng. Process. 42 (2003) 9–14.
[12] M.J.V. Goldschmidt, J.M. Link, S. Mellema, J.A.M. Juipers, Digital image analysis measurements of bed expansion and segregation dynamics in dense gas-fluidized beds, Powder Technol. 138 (2003) 135–159.
[13] L. Shen, F. Johnsson, B. Leckner, Digital image analysis of hydrodynamics two-dimensional bubbling fluidized beds, Chem. Eng. Sci. 59 (2004) 2607–2617.
[14] G.A. Bokkers, M. van Sint Annaland, J.A.M. Kuipers, Mixing and segregation in a bidisperse gas–solid fluidized bed: a numerical and experimental study, Powder Technol. 140 (2004) 176–186.
[15] W. Cheng, Y. Murai, T. Sasaki, F. Yamamoto, Bubble velocity measurements with a recursive cross correlation PIV technique, Flow Meas. Instrum. 16 (2005) 35–46.
[16] C. Zhu, Q. Yu, R.N. Dave, R. Pfeiffer, Gas fluidization characteristics of nanoparticle agglomerates, AIChE J. 51 (2) (2005) 426–439.
[17] X.S. Wang, V. Palero, J. Soria, M.J. Rhodes, Laser-based planar imaging of nano-particle fluidization. Part I. Determination of aggregate size and shape, Chem. Eng. Sci. 61 (2006) 5476–5486.
[18] C.N. Lim, M.A. Gilbertson, A.J.L. Harrison, Bubble distribution and behaviour in bubbling fluidized beds, Chem. Eng. Sci. 62 (2007) 56–69.
[19] J.G. Yates, d.D.J. Cheesman, Y.A. Sergeev, Experimental observations of voidage distribution around bubbles in a fluidized bed, Chem. Eng. Sci. 49 (1994) 1885–1895.
[20] L. Rizzuti, P.L. Yue, The measurement of light transmission through an irradiated fluidised bed, Chem. Eng. Sci. 38 (8) (1983) 1241–1249.
[21] P.L. Yue, L. Rizzuti, V. Augugliaro, Bubble phase voidage and dense phase voidage in thin two dimensional fluidized bed, Chem. Eng. Sci. 41 (1) (1986) 171–177.
[22] A. Brucato, L. Rizzuti, Simplified modelling of radiant fields in heterogeneous photoreactors. 1. Case of zero reflectance, Ind. Eng. Chem. Res. 36 (1997) 4740–4747.
[23] A. Brucato, L. Rizzuti, Simplified modelling of radiant fields in heterogeneous photoreactors. 2. Limiting "Two-Flux" model for the case of reflectance greater than zero, Ind. Eng. Chem. Res. 36 (1997) 4740–4755.
[24] J.N. Kapur, P.K. Sahoo, A.K. Wong, A new method for gray-level picture thresholding using the entropy of the histogram, Comput. Graphics Image Process. 29 (1985) 273–285.
[25] P.N. Rowe, C. Yacono, The distribution of bubble size in gas fluidised beds, Trans. Instn. Chem. Engrs. 53 (1975) 59.
[26] R.C. Darton, R.D. La Nauze, J.F. Davidson, D. Harrison, Bubble growth due to coalescence in fluidized beds, Trans. Instn. Chem. Engrs. 55 (1977) 274.
[27] J.F. Davidson, D. Harrison, Fluidized Particles, Cambridge University Press, 1963.